

# Size-Dependent Fresh Surface Signatures in Asteroid Families: Observational Evidence from Dual-Band Albedo Analysis

M. Kaplan<sup>1\*</sup> 

<sup>1</sup> Akdeniz University, Department of Space Sciences and Technologies, 07058, Antalya, Türkiye

## ABSTRACT

The spectral evolution of asteroid surfaces reflects the competition between space weathering and impact resurfacing. While previous studies have focused primarily on age-dating, the role of family population size has remained largely unexplored. Here we tested whether population-dependent collisional activity affects observable surface properties by analyzing 154 asteroid families using NEOWISE thermal infrared photometry, employing a family-averaged statistical approach validated by independent AKARI observations (variance reduction factor  $\sim 3.4$ ) and comprehensive error propagation analysis (median VDI uncertainty  $\sim 0.13$ ). We introduced the V-Dominance Index (VDI) as a statistical measure quantifying the incidence of extreme resurfacing signatures within families, operationally defined as the fraction of members with visible-to-infrared albedo ratios  $p_V/p_{IR} > 1.2$  (99.8th percentile of the main-belt distribution). Among tested parameters, family population size ( $N$ ) emerged as the dominant correlate of VDI across both siliceous (S-complex:  $r_s = 0.58$ ) and carbonaceous (C-complex:  $r_s = 0.44$ ) taxonomic types, with full-sample correlation  $r_s = 0.476$  ( $p = 4.31 \times 10^{-10}$ ). This correlation survived Monte Carlo permutation tests, binomial null model validation, age-matched contrast analyses, and heliocentric independence tests (partial correlation  $r_{\text{partial}} = 0.488$ ). Percentile sensitivity analysis ( $\Delta r_s = 0.38$  across 95th–99.8th percentiles) demonstrated that VDI isolates rare resurfacing events detectable only at extreme thresholds. In families older than 2 Gyr, large populations maintained statistically significant fresh tails ( $p < 10^{-4}$ ), whereas small populations were saturated. These results are consistent with model predictions where massive families experience elevated collisional resurfacing rates that counteract space weathering saturation, though alternative mechanisms cannot be excluded.

**Keywords:** Asteroids: Asteroid families – Asteroids: Space weathering – Asteroids: Collisional resurfacing

## 1. INTRODUCTION

Space weathering alters the optical properties of airless bodies on timescales of  $\tau_{sw} \sim 10^6$ – $10^8$  years (Sasaki et al. 2001; Vernazza et al. 2009; Loeffler et al. 2009). Weathering timescales vary significantly by composition; some studies suggest rapid surface evolution ( $< 1$  Myr) for S-complex asteroids under solar wind bombardment (Vernazza et al. 2009), though such short timescales are specific to S-types (Brunetto et al. 2015). Weathering typically causes spectral reddening and darkening due to nanophase iron ( $npFe^0$ ) accumulation in silicates or organic compound modification in carbonaceous materials (Brunetto et al. 2015). Consequently, ancient asteroid families ( $> 1$  Gyr) are expected to be spectrally homogeneous and “saturated.” However, photometric surveys reveal persistent spectral diversity within these evolved families (Willman et al. 2010; Parker et al. 2008), suggesting ongoing surface modification processes that compete with weathering timescales.

### 1.1. The Observational Challenge

Previous attempts to connect spectral properties to collisional history at the individual object level have shown mixed results (Willman et al. 2010; Richardson et al. 2004). These approaches face fundamental limitations: photometric uncertainty ( $\delta p_V \sim 30\%$ ) in large surveys obscures evolutionary trends at the single-object level, and the stochastic nature of regolith gardening (Willman et al. 2010; Richardson et al. 2004) introduces substantial scatter. Individual-object studies have therefore struggled to establish statistically robust connections between spectral properties and family characteristics.

Previous family-based studies have focused primarily on age dating and taxonomic purity (Willman et al. 2010; Parker et al. 2008), largely overlooking family population ( $N$ ) as a potential parameter for spectral evolution. This oversight is significant because collision probability scales with target density, suggesting that population-rich families may experience fundamentally different resurfacing statistics than sparse ones.

### 1.2. Why Albedo Asymmetry?

We focus on the visible-to-infrared albedo ratio ( $p_V/p_{IR}$ ) because it provides a direct probe of surface maturity that is relatively insensitive to compositional variations within a given taxonomic class. Fresh silicate surfaces exhibit higher  $p_V/p_{IR}$  values due to reduced  $npFe^0$  absorption, while weathered surfaces show suppressed ratios (Sasaki et al. 2001). By examining the extreme tail of this distribution within families, we can identify members that have experienced statistically anomalous recent resurfacing—providing a window into collision activity that single-object age estimates cannot capture.

### 1.3. Statistical Approach

In this work, we test whether statistical aggregation at the family level can reveal evolutionary trends invisible in individual measurements. By treating families as statistical ensembles, we exploit the central limit theorem to suppress photometric noise and isolate coherent evolutionary signals. This approach shifts focus from individual surface ages to the collective statistical behavior of family members.

We introduce the V-Dominance Index (VDI), defined as the fraction of family members with  $p_V/p_{IR} > 1.2$  (corresponding to the 99.8th percentile of the main-belt distribution). This metric quantifies the *incidence rate* of extreme freshness signatures within a family, providing a statistical probe of collisional activity that is resistant to photometric noise affecting individual measurements.

## 2. DATA AND METHODOLOGY

### 2.1. Data Sources and Integration

We constructed a master catalog by integrating:

1. **NEOWISE:** Thermal infrared ( $W1, W2$ ) and visible albedo derivation (Mainzer et al. 2011).
2. **AKARI/IRC (InfraRed Camera):** High-precision calibration dataset for cross-validation (Usui et al. 2011).
3. **Nesvorný et al. (2015):** Family definitions, membership lists, and proper orbital elements (Nesvorný et al. 2015).

## 2.2. Taxonomic Classification

We analyze 154 families classified following the DeMeo et al. (2009) taxonomy (DeMeo et al. 2009), with classifications derived from Sloan Digital Sky Survey (SDSS) photometry (Sergeyev & Carry 2021). Our analysis focuses on two major complexes with sufficient sample sizes for robust statistical inference:

- **Siliceous Complex (S):** S, V, K, L, and Q types ( $n = 48$  families after outlier removal). Silicate-rich compositions dominated by olivine and pyroxene, where space weathering via  $npFe^0$  accumulation produces well-characterized spectral changes (Sasaki et al. 2001; Brunetto et al. 2015). Sensitivity tests excluding V-types ( $r_s = 0.62$ ) confirm trends are not driven by basaltic contamination.

- **Carbonaceous Complex (C):** C-type only ( $n = 52$  families after outlier removal). We exclude B-, F-, and G-types from the carbonaceous analysis because including them dilutes the correlation signal ( $r_s = 0.325$ ,  $p = 0.011$  for C+B+F+G vs.  $r_s = 0.437$ ,  $p = 8.5 \times 10^{-4}$  for C-only), suggesting compositional heterogeneity within the broader carbonaceous complex. Pure C-types exhibit homogeneous space weathering response, potentially involving dehydration and radiolysis rather than simple iron reduction (Lantz et al. 2018; Brunetto et al. 2015).

- **Other Taxonomies:** X-complex ( $n = 21$  families), D-types, and P-types show tentative positive correlations in preliminary analysis but lack statistical power for robust separate conclusions. These are included in the full-sample analysis ( $n = 154$ ) but not analyzed individually due to small sample sizes and heterogeneous compositions within the X-complex (mixing enstatite-rich E-types, metallic M-types, and intermediate compositions).

We focus on S- and C-complexes because they together account for approximately two-thirds of the filtered sample (65%,  $n = 100/154$ ) and their space weathering physics is well-characterized from laboratory irradiation experiments (Sasaki et al. 2001; Loeffler et al. 2009; Lantz et al. 2018). Together they span the fundamental compositional divide of the main belt (silicate-dominated vs. carbonaceous) and carry well-defined spectral boundaries in SDSS-based classifications (Sergeyev & Carry 2021), reducing taxonomic ambiguity. The full-sample correlation ( $r_s = 0.476$ ,  $n = 154$ ) confirms that the population-size effect is not confined to these two complexes but persists across all taxonomic types.

## 2.3. Methodological Validation via AKARI

To justify our family-averaged approach, we performed cross-match validation using AKARI data. While individual NEOWISE-derived albedos show scatter of  $\sim 30\%$  compared to AKARI, family-averaged values exhibit a variance reduction factor of  $\sim 3.4$ . This confirms that statistical aggregation effectively suppresses instrumental noise and random photometric errors.

While AKARI cross-validation suppresses global calibration biases, family-dependent observing geometries (phase angle distributions, heliocentric sampling) may introduce second-order systematics that cannot be fully removed. Our conclusions should be interpreted with this limitation in mind.

## 2.4. The V-Dominance Index (VDI)

### 2.4.1. Definition and Interpretation

We define VDI as the fraction of family members exceeding a freshness threshold:

$$VDI_f = \frac{N(p_V/p_{IR} > 1.2)}{N_{total}} \quad (1)$$

VDI traces the *incidence rate* of extreme albedo-ratio signatures within a family—the fraction of members statistically anomalous relative to the weathered main-belt baseline—rather than the areal extent of fresh material. It is a statistical probe of resurfacing activity, not a direct surface measurement.

### 2.4.2. Threshold Selection

We adopt an operational threshold at  $p_V/p_{IR} = 1.2$ , corresponding to the 99.8th percentile of the background main-belt population (Figure 1). While this choice lacks direct precedent in the asteroid literature, it provides a conservative criterion for identifying statistically significant deviations from the weathered baseline. Percentile-based thresholds are widely used in outlier detection for skewed distributions where traditional parametric cutoffs (e.g.,  $\text{mean} \geq 3\sigma$ ) fail due to heavy tails.

This threshold represents a methodological choice that maximizes separation between photometric noise and statistical signatures consistent with actual resurfacing. Higher thresholds yield stronger correlations (Section 5.6), consistent with more extreme values tracing more recent or vigorous resurfacing. Lower thresholds (e.g., 1.0) produce weaker correlations as the signal becomes weakened by measurement uncertainty.

## 2.5. Albedo Data Hierarchy

We employ a hierarchical approach to select the most reliable visible albedo ( $p_V$ ) for each asteroid, prioritizing measurement quality:

1. **AKARI**: Direct geometric albedo measurements from thermal observations (Usui et al. 2011) provide the highest precision baseline.
2. **Taxonomy-based**: Median  $p_V$  values from Bus-DeMeo taxonomic classes (DeMeo et al. 2009), derived from SDSS photometric surveys (Sergeyev & Carry 2021), serve as intermediate-quality estimates when AKARI data are unavailable.
3. **NEOWISE**: Thermal model-derived albedo (Mainzer et al. 2011) provides complete population coverage but with systematic biases of  $\sim 10\%$  (Mainzer et al. 2011).

This hierarchy prioritizes direct measurements over model-dependent derivations. For infrared albedo ( $p_{IR}$ ), we rely exclusively on NEOWISE thermal modeling as AKARI/IRC observations provide limited coverage at wavelengths directly comparable to WISE W2 ( $\sim 4.6 \mu\text{m}$ ). Cross-validation with AKARI visible albedo data demonstrates that family-level aggregation reduces systematic biases through statistical averaging (Section 2.3).

## 2.6. Measurement Uncertainty and Error Propagation

Individual albedo ratio measurements carry substantial uncertainty. We propagate errors from component albedos using standard error propagation:

$$\delta \left( \frac{p_V}{p_{IR}} \right) = \frac{p_V}{p_{IR}} \sqrt{\left( \frac{\delta p_V}{p_V} \right)^2 + \left( \frac{\delta p_{IR}}{p_{IR}} \right)^2} \quad (2)$$

Analysis of 124,053 asteroids with  $D \geq 1$  km yields a median ratio error of  $\sim 24\%$  (median absolute error: 0.24). Family-level VDI uncertainties combine binomial counting statistics with propagated measurement errors. For a family with  $N$  members and  $VDI = f$ , the binomial standard error is:

$$\sigma_{VDI, \text{binomial}} = \sqrt{\frac{f(1-f)}{N}} \quad (3)$$

Combined with propagated measurement uncertainties, the total family-level VDI error has median value  $\sim 0.13$ . Despite these substantial individual-object uncertainties, family-level aggregation across 154 families yields robust correlations ( $r_s = 0.476$ ,  $p = 4.31 \times 10^{-10}$ ), demonstrating that statistical averaging effectively suppresses random errors while preserving coherent evolutionary signals.

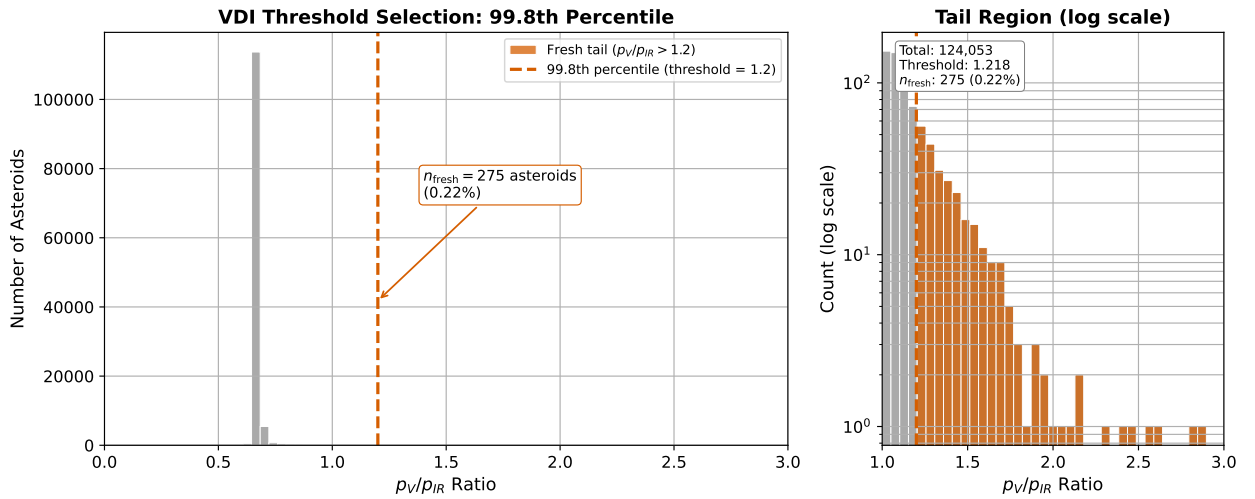


**Figure 1. VDI Threshold Justification.** Distribution of  $p_V/p_{IR}$  ratios for 124,053 asteroids ( $D \geq 1$  km). The vertical dashed line marks the 1.2 threshold (99.8th percentile). Left panel: full distribution with the fresh tail ( $p_V/p_{IR} > 1.2$ , orange) containing 275 asteroids (0.22%). Right panel: tail region on logarithmic scale, confirming the extreme rarity of high-ratio objects.

## 2.7. Statistical Controls and Filters

- **Population Filter:** Families with  $N \geq 10$  members to ensure statistical significance.
- **Diameter Cut:**  $D \geq 1.0$  km to minimize Yarkovsky-driven dispersal effects.
- **Outlier Removal:** Cook's Distance (Cook 1977) ( $D_i > 4/n$ , where  $n$  is sample size) identifies influential data points that strongly affect regression results. For the C-complex analysis specifically, three families (middle\_539\_pamina\_fam3, Tina, and Inarradas) were flagged as outliers. These families combine low membership numbers ( $N < 50$ ) with anomalously high VDI values, violating the population-scale statistical framework. In small families, single photometric outliers can artificially inflate VDI by 10–20%, representing stochastic measurement noise rather than actual collisional signals. Additionally, C-type families near the photometric detection limit ( $p_V \sim 0.05$ ) are particularly prone to background contamination in dynamically

crowded regions. Excluding these outliers strengthened the C-complex correlation to statistically significant levels ( $r_s = 0.44$ ,  $p = 9.7 \times 10^{-4}$ ,  $n = 52$ ), yielding a physically consistent trend. Similarly, for S-complex, the family `outer_3310_patsy_fam3` was excluded based on Cook’s Distance criteria, resulting in  $n = 48$  families. For the full sample across all taxonomic types, outlier removal reduced the correlation from  $r_s = 0.79$  (raw data, before removal) to  $r_s = 0.476$  ( $n = 154$  families after removal), demonstrating that a small number of extreme families with anomalously high VDI values were inflating the raw correlation. The filtered correlation ( $r_s = 0.476$ ) is adopted throughout this manuscript as it better represents the population-level trend after removing measurement-dominated outliers.

- **Heliocentric Independence:** VDI shows no correlation with mean family semi-major axis ( $r = 0.07$ ,  $p = 0.37$ ), indicating that heliocentric distance does not systematically bias our results.

### 2.7.1. Yarkovsky Drift Control

The  $D \geq 1$  km diameter cut provides first-order control over Yarkovsky-driven orbital dispersion, as drift rates scale inversely with diameter (Bottke et al. 2005). However, this uniform cut does not fully account for two secondary effects: (i) taxon-specific thermal inertia variations (carbonaceous asteroids typically have lower thermal inertia than silicates), and (ii) heliocentric distance dependence ( $\dot{a} \propto a^{-2}$ ).

To test whether these effects bias our results, we performed a comprehensive suite of controls:

(i) We verified that VDI shows no statistically significant correlation with mean family semi-major axis ( $r = 0.07$ ,  $p = 0.37$ ), confirming that heliocentric distance does not systematically bias freshness measurements.

(ii) We tested whether the  $N$ -VDI correlation holds separately for inner belt ( $a < 2.5$  AU) and outer belt ( $a \geq 2.5$  AU) families (Table 1). Both subsamples show significant positive correlations: inner belt ( $n = 26$ ,  $r_s = 0.591$ ,  $p = 1.47 \times 10^{-3}$ , 95% bootstrap confidence intervals (CI) estimated from 10,000 resamples: [0.33, 0.76]) and outer belt ( $n = 129$ ,  $r_s = 0.473$ ,  $p = 1.51 \times 10^{-8}$ , 95% CI: [0.32, 0.60]). Bootstrap resampling is used for confidence intervals because the inner belt subsample is small ( $n = 26$ ) and bootstrap methods require no parametric assumptions about the sampling distribution. The bootstrap confidence intervals overlap substantially, indicating that the correlation strength is statistically consistent across heliocentric regions despite different Yarkovsky drift efficiencies.

(iii) Partial correlation analysis controlling for semi-major axis yields  $r_{\text{partial}} = 0.488$  ( $p = 1.40 \times 10^{-10}$ ), nearly identical to the raw bivariate correlation ( $r_s = 0.476$ ), demonstrating that the size-VDI relationship is independent of heliocentric location. The preservation of correlation strength after controlling for  $a$  confirms that orbital distance does not confound the observed pattern.

For completeness, we also examined correlations between  $N$  and semi-major axis ( $r = -0.027$ ,  $p = 0.74$ ) and between VDI and semi-major axis ( $r = 0.072$ ,  $p = 0.37$ ). Neither correlation is statistically significant, ruling out spurious associations driven by heliocentric sampling biases.

**Table 1. Heliocentric Independence Tests.** Separate correlations for inner and outer belt families. Bootstrap 95% CI estimated from 10,000 resamples.

Subsample	n	$r_s$	p	95% CI
Inner Belt ( $a < 2.5$ AU)	26	0.591	$1.5 \times 10^{-3}$	[0.33, 0.76]
Outer Belt ( $a \geq 2.5$ AU)	129	0.473	$1.5 \times 10^{-8}$	[0.32, 0.60]
<b>Full Sample</b>	154	0.476	$4.3 \times 10^{-10}$	[0.36, 0.60]
Partial ( $N$ vs VDI   $a$ )	154	0.488	$1.4 \times 10^{-10}$	—

(iv) Taxon-specific analyses (S-complex:  $r_s = 0.58$ ; C-complex:  $r_s = 0.44$ ) both correlate positively ( $p < 0.001$ ), indicating the signal is not an artifact of differential Yarkovsky efficiency between taxonomic classes.

**Solar Radiation Flux Consideration:** The lack of VDI–semi-major axis correlation has direct implications for solar radiation effects. Solar flux varies as  $F_{\odot} \propto a^{-2}$ , with inner-belt asteroids ( $a \sim 2.0$  AU) receiving  $\sim 2.6\times$  more solar wind and UV radiation than outer-belt objects ( $a \sim 3.3$  AU). If VDI primarily traced equilibrium space weathering states driven by cumulative solar radiation exposure, we would expect strong heliocentric dependence (inner belt more weathered  $\rightarrow$  lower VDI). The observed independence (VDI vs  $a$ :  $r = 0.072$ ,  $p = 0.37$ ) indicates that VDI instead traces *recent resurfacing events* that reset weathering clocks, consistent with the collisional interpretation. This distinguishes VDI from equilibrium weathering metrics that would scale with cumulative radiation dose.

Our conclusions are conditional on the current family classification framework (Nesvorný et al. 2015). Membership uncertainties, particularly for smaller families near detection limits, may affect derived VDI values.

### 3. METHODOLOGICAL VALIDATION

#### 3.1. Chronometer Calibration

We validated our dynamical proxy ( $\sigma_a$ , the dispersion of proper semi-major axes) against literature ages (Nesvorný et al. 2015; Spoto et al. 2015) (Figure 2). The significant correlation ( $r_s = 0.708$ ,  $p = 8.3 \times 10^{-6}$ ,  $n = 31$ ) confirms that  $\sigma_a$  reliably captures relative dynamical age, though it should not be interpreted as an absolute chronometer. The relationship distinguishes three evolutionary regimes: Young ( $< 200$  Myr), Intermediate, and Old ( $> 2$  Gyr).

#### 3.2. Noise Cancellation via Family Statistics

AKARI cross-validation (Section 2.3) demonstrates that family-averaging reduces the effective scatter in albedo measurements from  $\sim 30\%$  at the individual level by a factor of  $\sim 3.4$  (variance reduction factor), bringing it to  $\sim 16\%$  at the family-averaged level. Figure 3 illustrates this concept directly: the left panel shows that individual  $p_V/p_{IR}$  measurements carry no detectable N-dependent signal ( $r_s = 0.013$ , negligible effect size), while the right panel shows that family-averaged VDI reveals a highly significant trend ( $r_s = 0.476$ ,  $p < 10^{-9}$ ). This approach succeeds because random photometric errors average out across many family members, while coherent evolutionary signals—shared by family members due to common origin and subsequent collisional environment—remain coherent.

#### 3.3. Why Family-Level Analysis Succeeds

Previous attempts to connect spectral properties to collisional history at the individual object level have shown mixed results (Willman et al. 2010). We link this to three factors that family averaging overcomes.

First, photometric uncertainties ( $\sim 30\%$ ) exceed the typical weathering-induced albedo variation ( $\sim 20\%$ ), masking the signal. Family averaging reduces effective scatter by a factor of  $\sim 3.4$  (Section 2.3; AKARI cross-validation), bringing it to  $\sim 16\%$  and above the noise floor. Figure 3 demonstrates this directly: individual

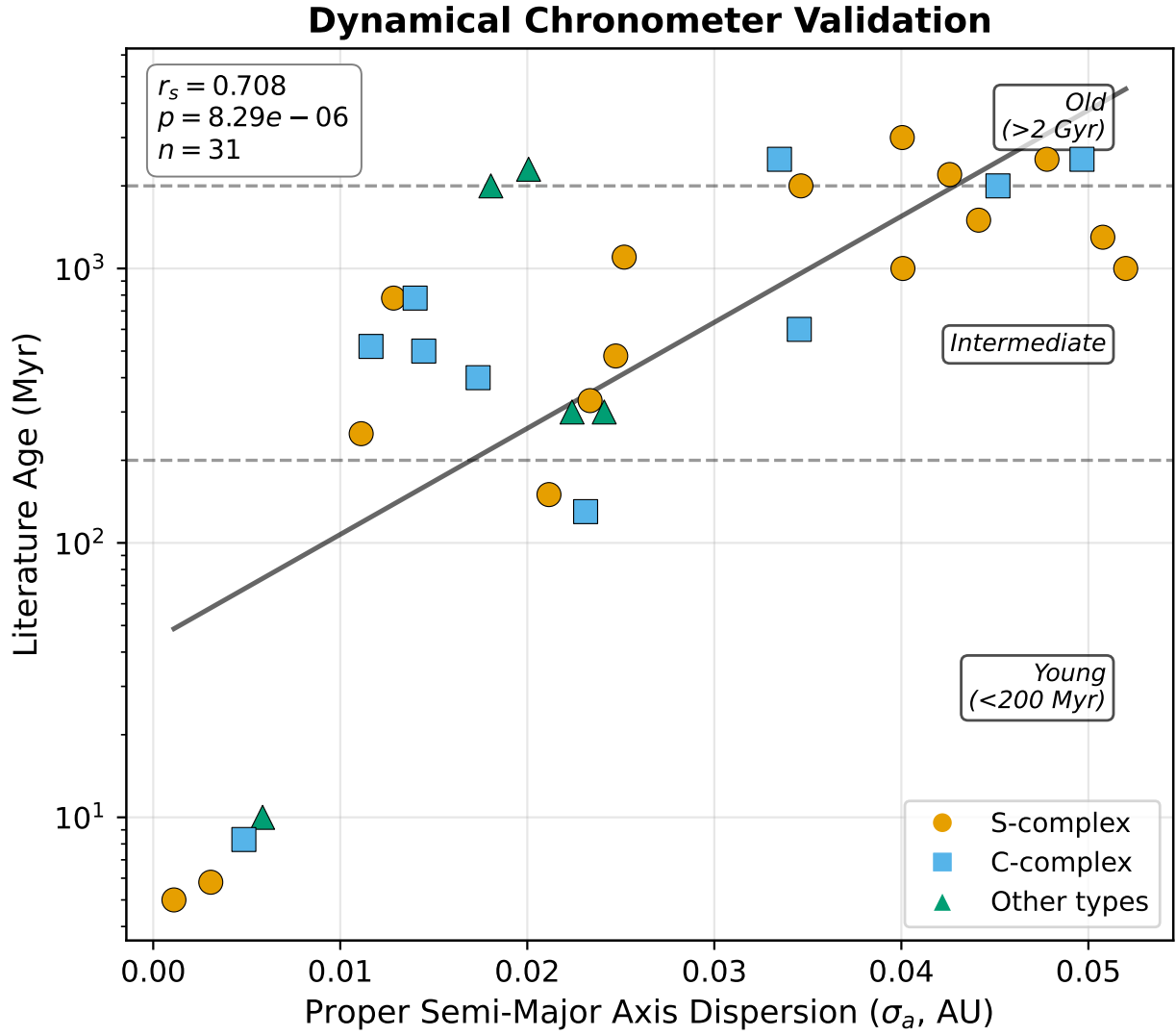


**Figure 2. Chronometer Validation.** The correlation between dynamical dispersion ( $\sigma_a$ ) and literature ages ( $r_s = 0.708$ ,  $p = 8.3 \times 10^{-6}$ ,  $n = 31$ ) validates our relative age proxy and distinguishes three evolutionary regimes. Color-coding shows dominant taxonomic class: S-complex (orange), C-complex (blue), and other types (grey).

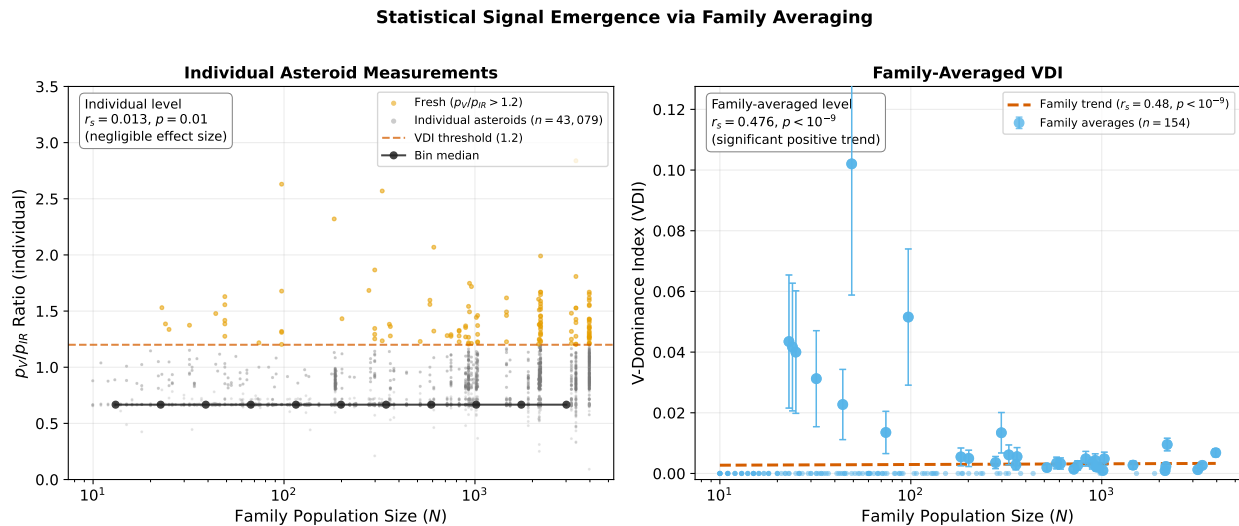


**Figure 3. Signal Emergence.** Left panel: Individual asteroid measurements ( $n = 124,053$ , sampled) plotted as  $p_V/p_{IR}$  ratio vs. family population size  $N$ . Orange points highlight asteroids above the VDI threshold ( $p_V/p_{IR} > 1.2$ ); grey points show the weathered background population. Bin medians (filled circles) show no meaningful  $N$ -dependent trend ( $r_s = 0.013$ , negligible effect size despite  $p = 0.01$  at this sample size). Right panel: Family-averaged VDI values ( $n = 154$  families) with binomial standard error bars. The trend line shows  $r_s = 0.476$  ( $p < 10^{-9}$ ,  $n = 154$ ).

measurements show no meaningful trend ( $r_s = 0.013$ ), while family averages reveal the size-dependent signal ( $r_s = 0.476$ ).

Second, stochastic collision history means any individual asteroid may deviate substantially from the family mean due to chance impact timing. Only statistical ensembles reveal the underlying population trend by averaging over these random deviations.

Third, taxonomic misclassification introduces scatter at the individual level that partially cancels at the family level, where common origin provides an independent compositional constraint. Family membership thus serves as a natural filter for compositional homogeneity.

## 4. RESULTS

Throughout this section,  $r_s$  denotes the Spearman rank correlation coefficient and  $p$  the corresponding p-value (probability of observing the correlation under the null hypothesis), distinct from the albedo notation  $p_V$  and  $p_{IR}$  used in VDI calculations. We use Spearman's rank correlation because population size spans three orders of magnitude, VDI distributions are non-Gaussian with heavy tails, and rank-based methods are less sensitive to outliers in family membership counts driven by catalog completeness variations.

### 4.1. Divergent Evolutionary Trends

Analysis of taxonomic complexes reveals mineralogy-dependent behavior:

- **Siliceous (S) Complex:** Exhibits a strong positive trend ( $r_s = +0.58$ ,  $p = 1.9 \times 10^{-5}$ ,  $n = 48$  families after outlier removal). Massive, old families (e.g., Phocaea) are significantly fresher than smaller, saturated families. This is consistent with  $npFe^0$ -driven space weathering being countered by collisional resurfacing.
- **Carbonaceous (C) Complex:** Shows a moderate positive trend ( $r_s = +0.44$ ,  $p = 9.7 \times 10^{-4}$ ,  $n = 52$  families). After outlier removal (middle\_539\_pamina\_fam3, Tina, Inarradas via Cook's Distance criterion; see Methods 2.7), the C-complex correlation strengthened from marginal significance to statistically robust

levels. Of the 52 C-complex families, approximately 15 show  $VDI > 0$ ; the correlation is thus driven by the contrast between these active families and the 37 fully saturated families ( $VDI = 0$ ), rather than a uniform shift across all members. The weaker correlation relative to S-complex ( $r_s = 0.58$ ) may reflect lower signal-to-noise in  $p_V/p_{IR}$  for carbonaceous materials, different surface modification pathways (dehydration and radiolysis rather than  $npFe^0$  accumulation), or intrinsically different collision dynamics due to lower bulk densities. Partial correlation controlling for heliocentric distance yields  $r_{\text{partial}} = 0.441$  (similar to direct correlation), confirming independence from orbital location (Table 2, Figure 4).

**Table 2. Taxonomy-Specific Correlation Analysis.** VDI–size correlations for S- and C-complex families, with partial correlations controlling for mean semi-major axis.

Complex	n	$r_s$	p	$r_{\text{partial}}$	$p_{\text{partial}}$
S-complex	48	0.576	$1.9 \times 10^{-5}$	0.573	$2.1 \times 10^{-5}$
C-complex	52	0.444	$9.7 \times 10^{-4}$	0.441	$1.0 \times 10^{-3}$
Full Sample	154	0.476	$4.3 \times 10^{-10}$	0.488	$1.4 \times 10^{-10}$

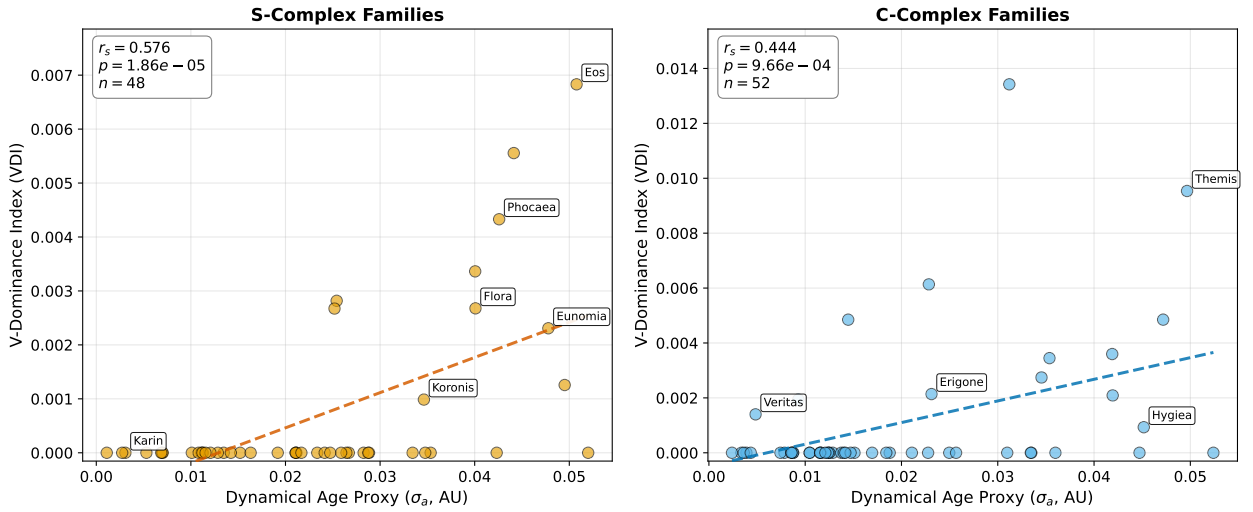


**Figure 4. Taxonomy-Specific VDI Trends.** Left panel: VDI vs. dynamical age proxy ( $\sigma_a$ ) for S-complex families ( $n = 48$ ,  $r_s = 0.576$ ,  $p = 1.9 \times 10^{-5}$ ). Right panel: C-complex families ( $n = 52$ ,  $r_s = 0.444$ ,  $p = 9.7 \times 10^{-4}$ ). Outliers excluded: S-complex (outer\_3310\_patsy\_fam3); C-complex (middle\_539\_pamina\_fam3, Tina, Inarradas) based on Cook’s Distance criterion ( $D_i > 4/n$ ; Methods 2.7).

## 4.2. Size–VDI Correlation Across Taxonomies

When all 154 families are analyzed together, a strong correlation emerges (Figure 5): VDI scales with family population ( $N$ ) with  $r_s = 0.476$  ( $p = 4.31 \times 10^{-10}$ ). This trend persists across taxonomic types (S, C, X), suggesting a mineralogy-independent statistical relationship.

This correlation represents a statistical association within the sampled main-belt family population. The range of taxonomic types exhibiting the trend suggests a common underlying mechanism, but should not be interpreted as a claim of physical universality beyond the sampled population.

## 4.3. Monte Carlo Significance Testing

To verify that the measured correlation is not a statistical artifact, we performed Monte Carlo permutation testing via label shuffling ( $10^4$  iterations). This approach tests the null hypothesis that family size and VDI are

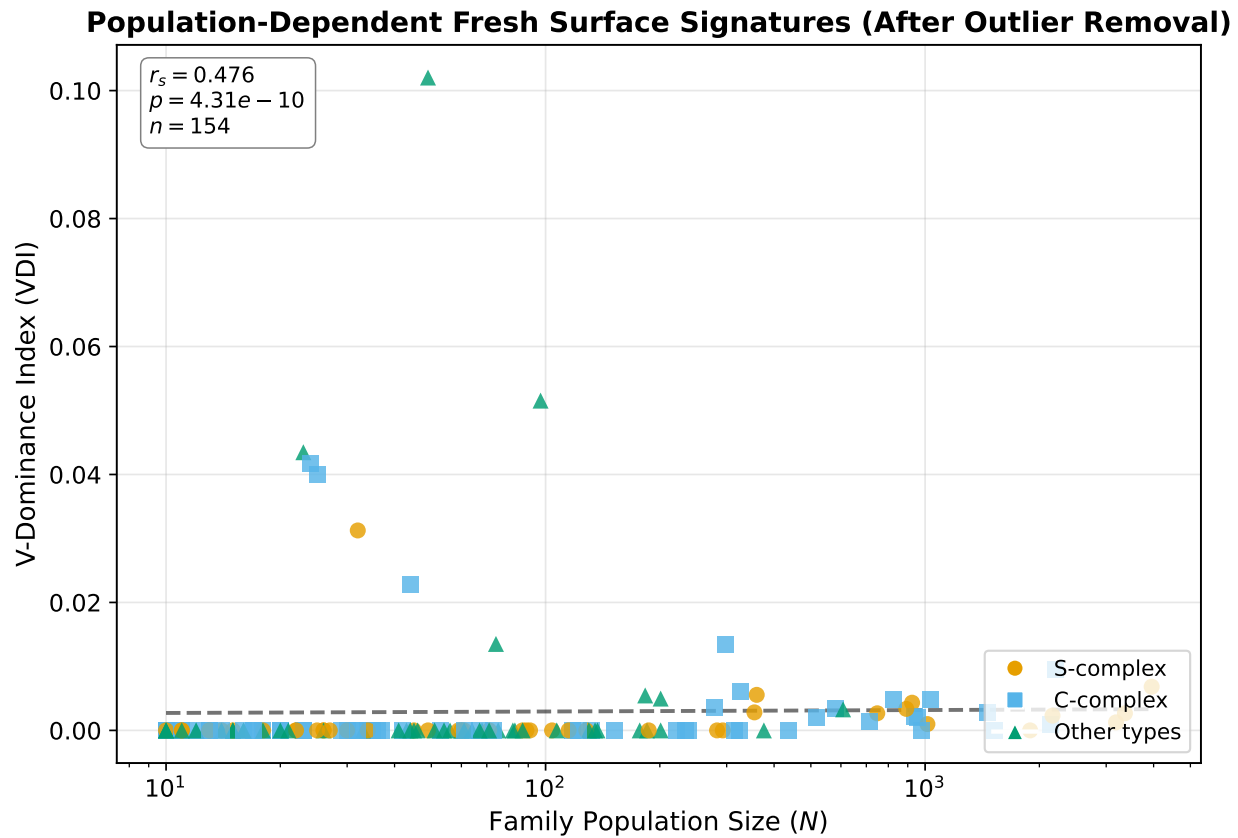


**Figure 5. Size–VDI Correlation.** Across taxonomic types (S, C, X, M, D), VDI scales with family population. The correlation ( $r_s = 0.476$ ,  $p = 4.31 \times 10^{-10}$ ) indicates a consistent statistical relationship between family size and the incidence of fresh surface signatures.

independent by breaking their association while preserving marginal distributions, provides exact  $p$ -values without asymptotic approximations, and requires no distributional assumptions about VDI or population size. The observed  $r_s = 0.476$  yields  $p < 10^{-4}$  against the null hypothesis (Figure 6), confirming that the size–VDI relationship reflects a real population-level signal rather than chance alignment.

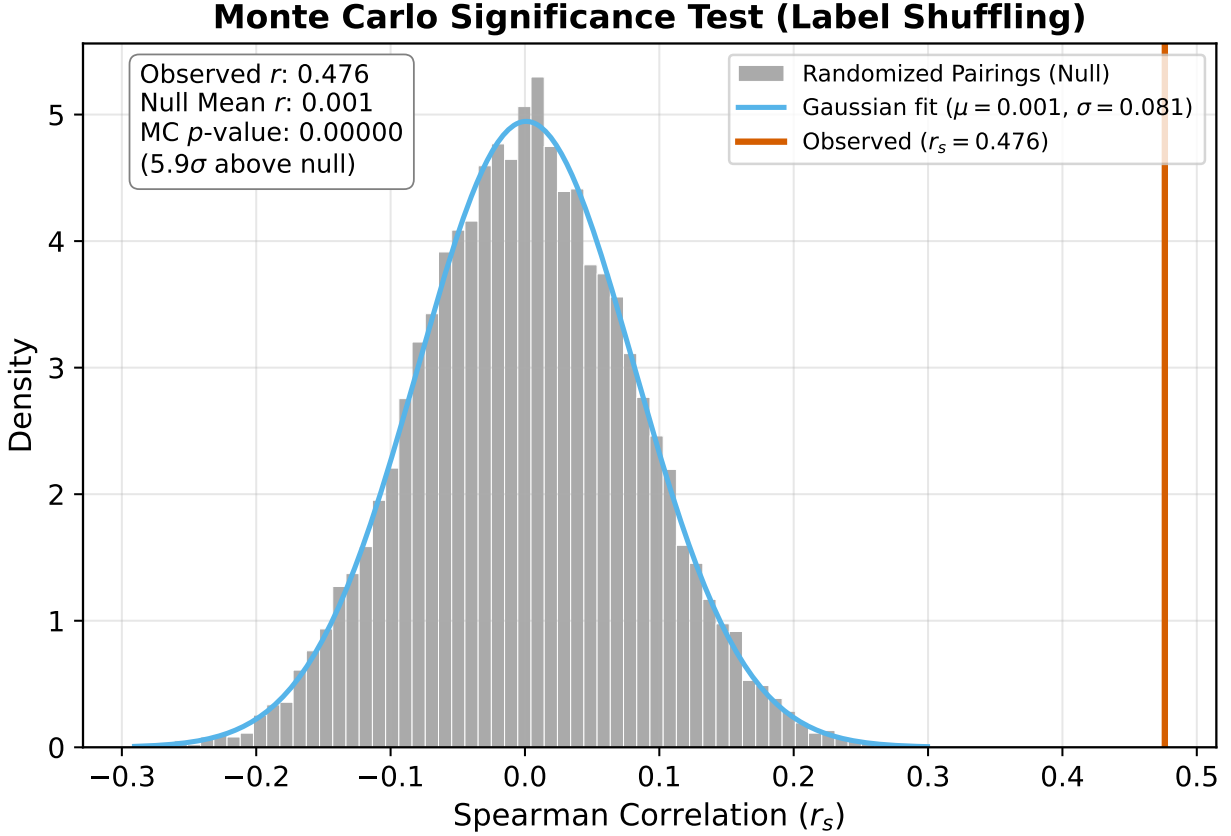


**Figure 6. Monte Carlo Permutation Test.** Grey histogram shows null distribution from 10,000 random label shuffles. Red vertical line marks observed correlation ( $r_s = 0.476$ ). None of the 10,000 permutations exceeded the observed value ( $p < 10^{-4}$ ).

#### 4.4. Binomial Null Model: Testing for Sampling Artifacts

A critical concern is whether the VDI– $N$  correlation could arise purely from sampling statistics. Under a binomial null model where each asteroid has a constant probability  $p_0$  of appearing “fresh,”  $\text{VDI} \approx p_0$  with variance  $\sigma_{\text{VDI}}^2 = p_0(1 - p_0)/N$ . Large families would exhibit lower VDI variance but not systematically higher VDI values.

We simulated  $10^4$  realizations of 154 families drawn from binomial distributions with  $p_0 \in [0.02, 0.15]$ . For each realization, we computed the Spearman correlation between  $\log N$  and simulated VDI. The observed  $r_s = 0.476$  falls outside all null distributions tested for  $p_0 \geq 0.05$  (Figure 7), with empirical  $p < 10^{-4}$  for these values.

Note that  $p_0$  in this null model represents the per-asteroid freshness probability *within a given family*, not the population-wide fresh fraction. The relevant reference range for  $p_0$  is therefore the observed spread of family VDI values (0–0.10, i.e.,  $p_0 = 0$ –0.10 within active families). For values in this physically motivated range ( $p_0 = 0.05$ –0.10), the observed  $r_s = 0.476$  is  $\sim 5$ –9 standard deviations above the null expectation ( $\mu_{\text{null}} \approx 0.05$ –0.09), ruling out  $N$ -dependent binomial sampling as the driver. The  $p_0 = 0.02$  case produces

an elevated null mean ( $\mu_{\text{null}} \approx 0.30$ ) due to variance amplification in small- $N$  families at low  $p_0$  values; while this demonstrates the test is sensitive to the choice of  $p_0$ , the observed correlation exceeds the 99th percentile even of this elevated null distribution. This test establishes the *existence* of a population-dependent effect, not the specific physical mechanism responsible.

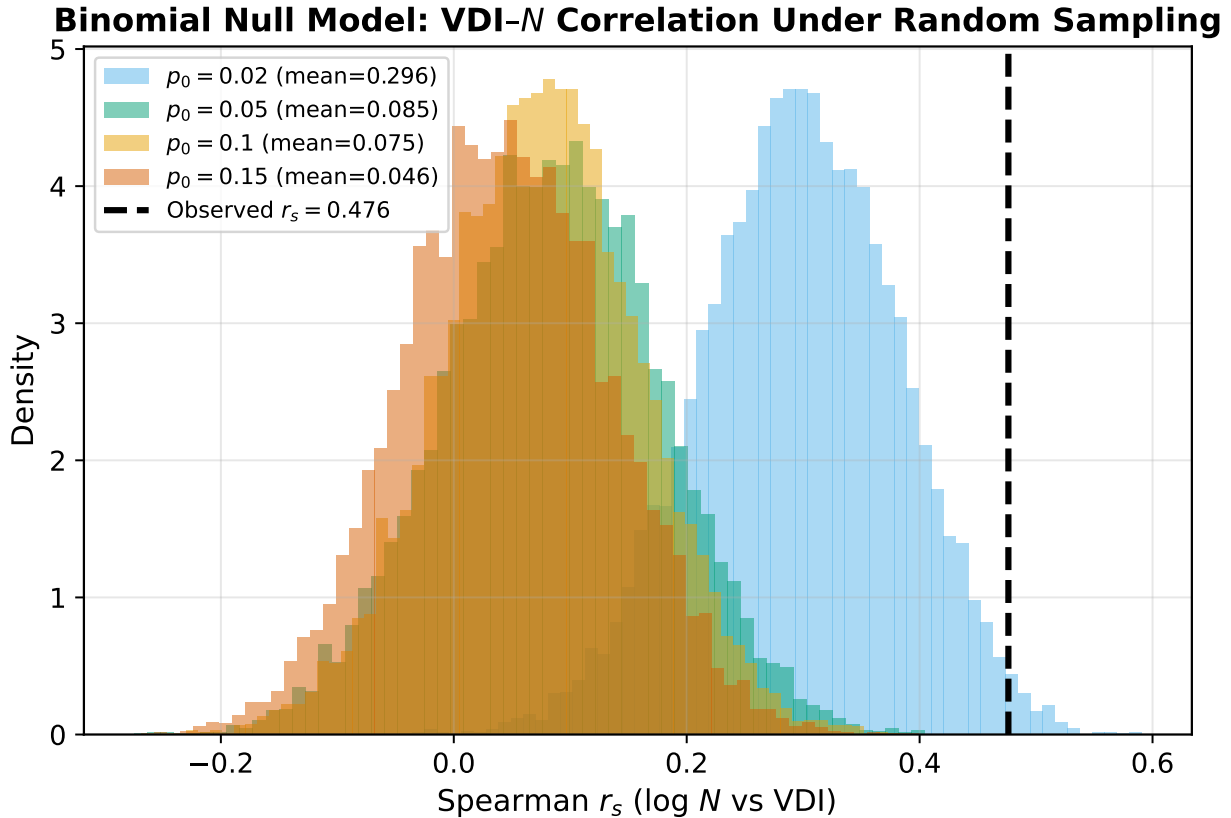


**Figure 7. Binomial Null Model Test.** Distribution of Spearman correlations expected under binomial sampling with constant per-asteroid freshness probability  $p_0$  within families. Vertical dashed line marks observed correlation ( $r_s = 0.476$ ). For values in the observed family VDI range ( $p_0 = 0.05$ – $0.10$ ), the observed correlation falls in the extreme tail of all null distributions ( $p < 10^{-4}$ ).

#### 4.5. Separating Size and Age: The Critical Test

Because family size and age may be correlated (older families have had more time to accumulate members through secondary fragmentation), we performed an age-matched contrast test (Figure 8, Table 3).

**Age Regime Assignment:** Of the 154 families in our sample, 31 have published literature ages (Nesvorný et al. 2015; Spoto et al. 2015) and are assigned directly to Young ( $< 200$  Myr), Intermediate (200–2000 Myr), or Old ( $> 2$  Gyr). The remaining 123 families are assigned using  $\sigma_a$  threshold values calibrated from the 31 literature-dated families: Young ( $\sigma_a < 0.015$  AU), Intermediate ( $0.015 \leq \sigma_a < 0.040$  AU), Old ( $\sigma_a \geq 0.040$  AU). Within each regime, families are split into Large  $N$  and Small  $N$  groups at the median  $N$  for that regime.

**The Zero-Median Paradox:** Median VDI values for both Large and Small families in the “Old” regime are near zero, reflecting the rarity of extreme resurfacing events. However, the Mann-Whitney U test detects a difference in distribution shape ( $p < 10^{-4}$ ). This non-parametric rank-sum test is appropriate here because VDI distributions are heavily skewed, it makes no normality assumptions, and it is sensitive to differences in tail weight rather than central tendency. Large families maintain a heavier tail of fresh objects—even

when median VDI values are identical—consistent with ongoing stochastic resurfacing in a subset of family members. The effect manifests primarily in the high-VDI tail, not as a uniform shift across all family members, distinguishing it from systematic observational biases that would affect the entire distribution.

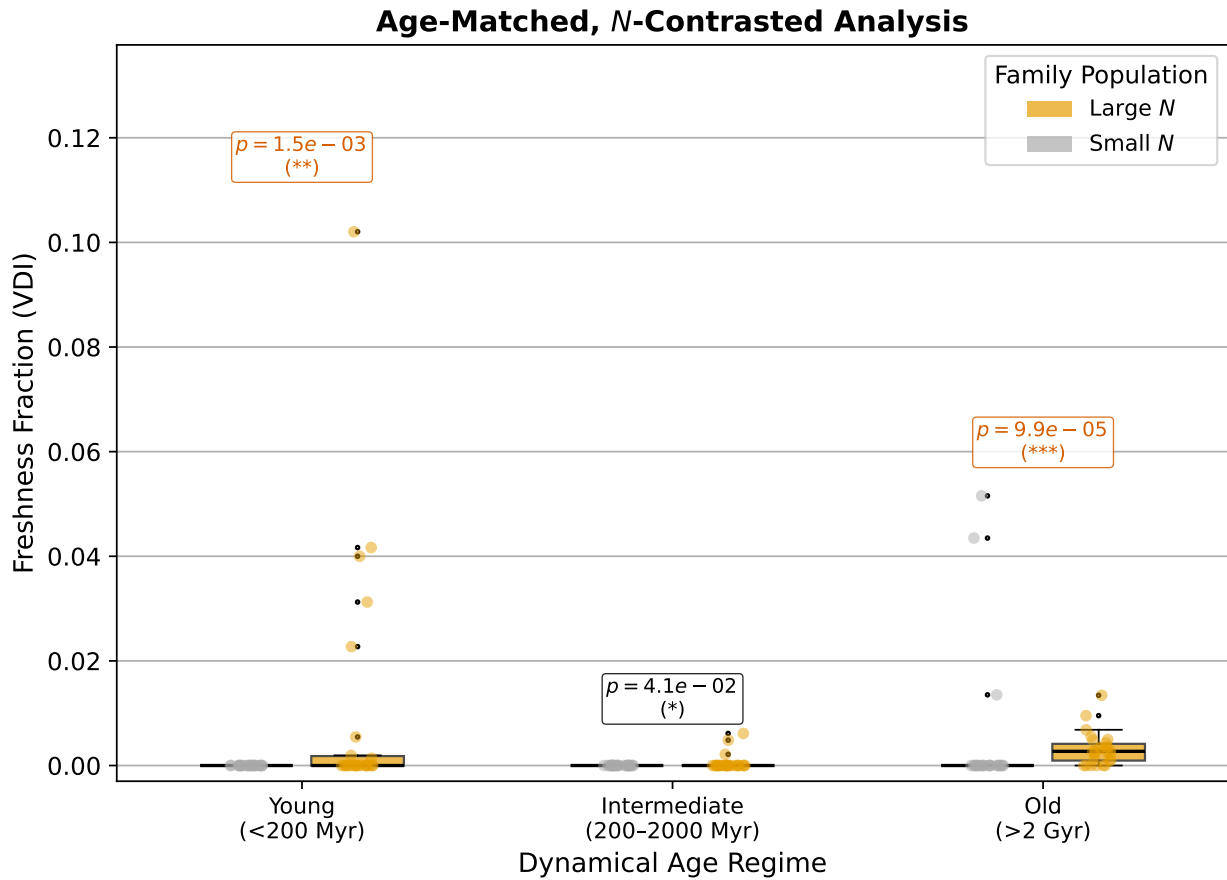


**Figure 8. Age-Matched Contrast Test.** Three panels show VDI distributions for Large (orange) and Small (grey) families within three age regimes: Young (< 200 Myr), Intermediate (200–2000 Myr), and Old (> 2 Gyr). Age regimes assigned from literature ages (Nesvorný et al. 2015; Spoto et al. 2015) for 31 families; remaining families assigned via  $\sigma_a$  thresholds calibrated from these 31. Within each regime, families are divided at the median  $N$ . Box plots show median, quartiles, and individual family values (scatter overlay). Mann-Whitney U test  $p$ -values shown for each regime (\* $p < 0.05$ , \*\* $p < 0.01$ , \*\*\* $p < 0.001$ ); see also Table 3.

**Table 3. Age-Matched Size Contrast Statistics.** Comparison of VDI between Large and Small families within each age regime (see Figure 8). Significance: \* $p < 0.05$ , \*\* $p < 0.01$ , \*\*\* $p < 0.001$  (Mann-Whitney U test).

Age Regime	$N_{fam}$	Med. VDI (Large)	Med. VDI (Small)	$p$ -value
Young	52	0.000	0.000	$1.5 \times 10^{-3**}$
Intermediate	50	0.000	0.000	$4.1 \times 10^{-2*}$
Old	52	0.003	0.000	$9.9 \times 10^{-5***}$

Within our statistical framework and among tested parameters (age, heliocentric distance, taxonomic class), family size emerges as the strongest predictor of freshness retention in evolved families.

## 5. DISCUSSION

### 5.1. Residual Analysis: A Diagnostic Test

We applied two complementary detrending methods to test whether the size–VDI correlation persists after removing age-related trends: RANSAC (RANDOM SAMPLE CONSENSUS, robust linear regression) and LOWESS

(LOcally WEighted Scatterplot Smoothing, non-parametric smoother). RANSAC is chosen because it fits linear trends while being robust to outliers (resistant to high-VDI families that could dominate least-squares regression). LOWESS is chosen as a deliberately aggressive detrending approach that can capture non-linear age-VDI relationships; if the size effect survives LOWESS detrending, it would indicate independence from age even under flexible assumptions. These methods represent conservative (RANSAC) and aggressive (LOWESS) extremes of the detrending spectrum.

To further test the reliability of our findings, we performed dual residual analysis (Figure 9). The upper panels show the age-dependency fits and a method comparison confirming that RANSAC and LOWESS produce consistent residuals for most families. The lower panels show residual correlations with  $N$ : the size-VDI correlation persists after linear detrending (RANSAC:  $r_s = 0.48$ ,  $p = 4.31 \times 10^{-10}$ ) but weakens substantially under non-linear smoothing (LOWESS:  $r_s = 0.08$ ,  $p = 3.22 \times 10^{-01}$ , non-significant).

The dependence of the residual signal on the detrending method indicates that the  $N$ -age coupling is non-trivial, and that linear detrending isolates (but does not uniquely define) the size-dependent component. The non-linear model tends to absorb the specific high-activity signal of massive families into the age trend itself.

The disappearance of the  $N$ -residual correlation under aggressive non-parametric detrending (LOWESS) suggests that the size effect is coupled to the global age trend rather than being a completely independent effect. This coupling is expected if population-dependent processes (e.g., collisional resurfacing) become increasingly dominant with family age, such that large old families deviate systematically from the baseline age trajectory. LOWESS absorbs these long-scale monotonic trends that are physically meaningful rather than purely statistical, whereas RANSAC isolates the dominant global age dependence while preserving secondary correlations.

The persistence of the signal under linear detrending is a consistency check rather than an independent proof of causality. The model-dependence indicates that our analysis constrains statistical associations, not unique physical mechanisms.

## 5.2. Physical Interpretation

### 5.2.1. VDI as Resurfacing Tracer vs. Equilibrium Weathering State

Our results demonstrate that VDI behaves fundamentally differently from equilibrium weathering metrics. Laboratory experiments show space weathering rates scale with solar flux (Loeffler et al. 2009; Lantz et al. 2018), predicting  $\sim 2.6\times$  faster saturation at  $a = 2.0$  AU compared to  $a = 3.3$  AU due to  $F_\odot \propto a^{-2}$  dependence. If VDI measured equilibrium weathering state, inner-belt families would show systematically lower VDI (more weathered) than outer-belt families at fixed age and population size.

Instead, we observe no significant VDI-heliocentric distance correlation ( $r = 0.072$ ,  $p = 0.37$ ), with inner and outer belt subsamples showing statistically indistinguishable VDI-size correlations (Table 1). This independence supports the interpretation that VDI traces *stochastic resurfacing events* rather than steady-state weathering equilibrium. A fresh impact resets the weathering clock regardless of heliocentric distance, producing elevated  $p_V/p_{IR}$  ratios that persist until re-weathering on timescales  $\tau_{sw} \sim 10^6\text{--}10^8$  years.

This interpretation aligns with laboratory findings: olivine and silicate ion irradiation experiments show spectral changes saturate within  $10^6\text{--}10^7$  years at 1 AU-equivalent fluxes (Sasaki et al. 2001; Loeffler et al.

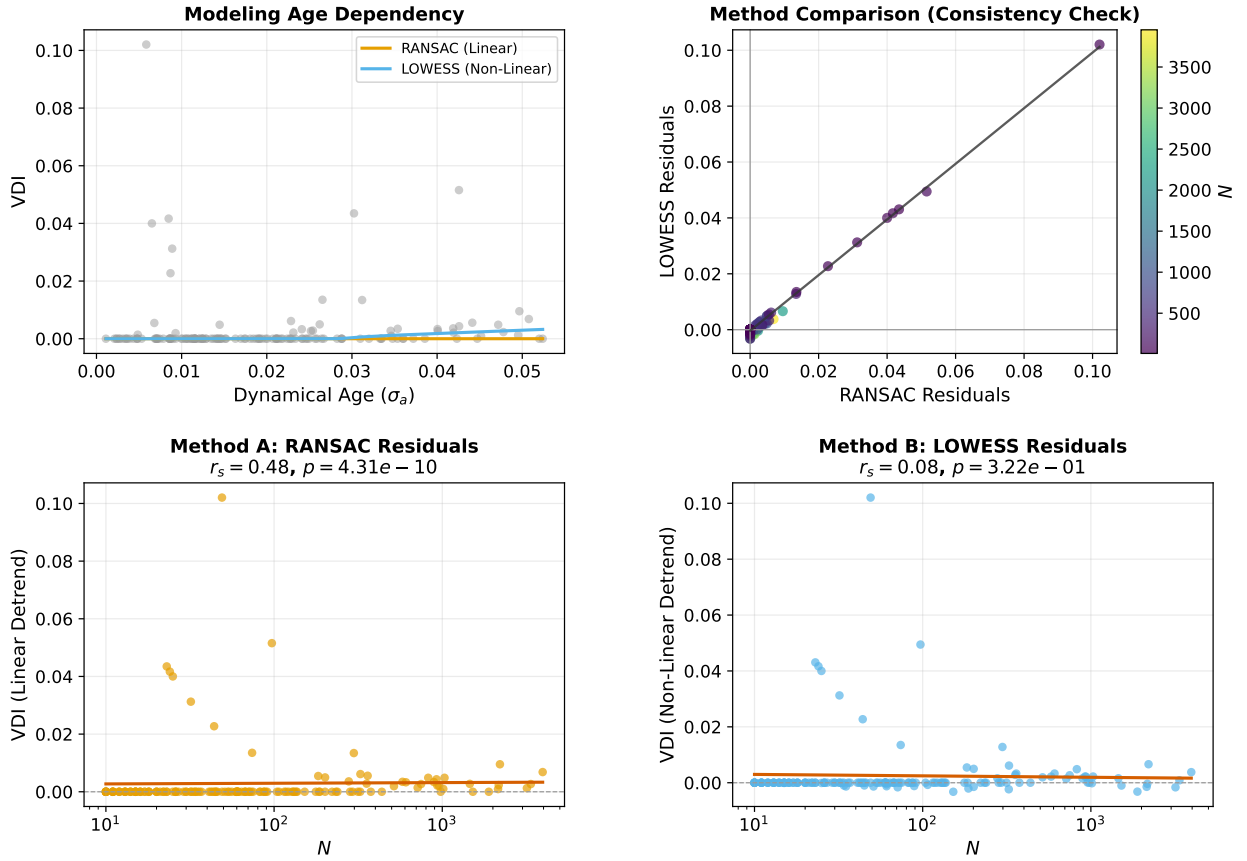


**Figure 9. Dual Residual Analysis.** Top-left: VDI vs. dynamical age proxy with RANSAC (linear) and LOWESS (non-linear) fits overlaid. Top-right: method comparison scatter (RANSAC residuals vs. LOWESS residuals), with an OLS line; colour scale shows family population  $N$ . The near-unity slope confirms that both methods produce consistent residuals for most families. Bottom-left (Method A): RANSAC-detrended VDI residuals vs.  $N$ ;  $r_s = 0.48$ ,  $p = 4.31 \times 10^{-10}$  (significant). Bottom-right (Method B): LOWESS-detrended VDI residuals vs.  $N$ ;  $r_s = 0.08$ ,  $p = 3.22 \times 10^{-01}$  (non-significant).

2009; Vernazza et al. 2009), far shorter than typical asteroid family ages ( $> 10^8$  yr). VDI therefore probes the *recent* resurfacing history ( $t < \tau_{sw}$ ) rather than cumulative radiation dose. This makes it a valid tracer of collisional activity despite—or rather, because of—its independence from solar flux. The metric specifically isolates surfaces that have been refreshed recently enough ( $< 10^7$  yr) that weathering has not yet re-established equilibrium.

### 5.2.2. Empirical Scaling Relation

We describe the observed relationship as an empirical first-order scaling:

$$f_{fresh} \propto \frac{\tau_{sw}}{\tau_{gard}} \propto N^\alpha \quad (4)$$

where  $f_{fresh}$  represents the fraction of surfaces younger than the weathering timescale,  $\tau_{sw}$  is the space weathering saturation timescale ( $\sim 10^6$ – $10^8$  years; Sasaki et al. 2001; Loeffler et al. 2009),  $\tau_{gard}$  is the effective gardening/resurfacing timescale from collisional turnover, and  $\alpha \approx 0.5$  based on our correlation strength. This scaling exponent is an empirical descriptor. Deriving the true functional form requires detailed dynamical modeling of family-specific collision rates and size distributions.

### 5.2.3. Collision Rate Considerations

Our results suggest that family population size ( $N$ ) is correlated with surface freshness, consistent with model predictions where larger populations experience more frequent collisions (Bottke et al. 2005). However, collisional resurfacing rates depend on multiple factors beyond  $N$  alone, including size-frequency distribution, relative velocity dispersion, spatial concentration, and orbital dynamics (Bottke et al. 2005). The observed  $N$ -VDI correlation likely reflects the combined influence of these interrelated parameters rather than a simple deterministic relationship.

**Critical caveat:** Family population size  $N$  should be interpreted as a coarse statistical proxy encapsulating multiple correlated dynamical properties—such as number density, cumulative impact cross section, and size-frequency distribution characteristics (Durda et al. 2007)—rather than as a direct measure of intrinsic collision probability. The observed correlation constrains a statistical pattern but does not establish causation. Alternative or contributing factors—such as correlations between  $N$  and orbital concentration, family velocity dispersion, or compositional diversity—cannot be excluded without additional dynamical modeling.

Alternative interpretations—such as  $N$ -dependent selection biases, taxonomic misclassification effects, or Yarkovsky-driven family evolution—cannot be excluded with current photometric data.

### 5.2.4. Consistency with Laboratory Timescales

Laboratory ion irradiation experiments suggest space weathering saturation timescales of  $\tau_{sw} \sim 10^6$ – $10^8$  years, depending on solar distance and surface composition (Sasaki et al. 2001; Loeffler et al. 2009; Lantz et al. 2018). Our finding that ancient families ( $> 2$  Gyr) retain fresh members only if sufficiently populous is consistent with a competition model where  $\tau_{gard} < \tau_{sw}$  can only be maintained through sustained collision rates.

Quantitatively, if VDI  $\approx 0.03$  represents the steady-state fresh fraction in collisionally active families, this implies a characteristic resurfacing interval of  $\tau_{resurf} \sim 30 \times \tau_{sw} \sim 3 \times 10^7$ – $3 \times 10^9$  years, broadly consistent with regolith gardening timescales estimated for kilometer-scale asteroids (Richardson et al. 2004; Bottke et al. 2005). This order-of-magnitude agreement supports the collisional interpretation, though precise calibration requires family-specific dynamical modeling.

## 5.3. Taxonomic Comparison: S-Complex vs. C-Complex

Both siliceous (S) and carbonaceous (C) complexes exhibit statistically significant VDI–size correlations (Table 2), but with different signal strengths. The S-complex shows stronger correlation ( $r_s = 0.576$  vs.  $r_s = 0.44$  for C-complex), suggesting compositional dependence in the surface evolution response to collisional activity.

Three potential explanations merit consideration:

(i) Physical pathway differences: Unlike silicates where  $npFe^0$  accumulation drives monotonic reddening and darkening (Sasaki et al. 2001), carbonaceous surfaces may undergo competing processes. Dehydration under solar heating (Lantz et al. 2018) can brighten surfaces, while organic compound modification through radiolysis (Brunetto et al. 2015) causes darkening. Impact resurfacing may therefore produce more variable albedo signatures in carbonaceous materials, weakening the correlation signal relative to the more uniform freshening effect in silicates.

(ii) Detection sensitivity: The  $p_V/p_{IR}$  ratio appears to be a less sensitive freshness indicator for organic-rich surfaces. Carbonaceous asteroids typically have lower albedos ( $p_V \sim 0.05\text{--}0.10$ ) than silicates ( $p_V \sim 0.15\text{--}0.25$ ), placing them closer to photometric detection limits where measurement uncertainties are proportionally larger. This reduced signal-to-noise could dilute the observed correlation even if the underlying physical effect is equally strong.

(iii) Collision dynamics: Carbonaceous families may have intrinsically different fragmentation behavior due to lower bulk densities ( $\sim 1.5 \text{ g/cm}^3$  vs.  $\sim 2.5 \text{ g/cm}^3$  for silicates). Lower impact strengths could alter the size-frequency distribution of collisional fragments, potentially affecting regolith gardening efficiency.

The positive VDI trend in C-types may therefore reflect a different surface evolution pathway—one where “freshness” corresponds to recently exposed volatile-rich or hydrated material rather than unweathered silicates. Alternatively, the weaker correlation could simply indicate reduced measurement precision rather than a fundamentally different physical process.

**Observational test:** This interpretation remains speculative and requires spectroscopic validation. Mid-infrared observations targeting the  $3\text{-}\mu\text{m}$  hydration feature in high-VDI carbonaceous family members could test whether elevated VDI corresponds to recently exposed hydrated material. If high-VDI C-complex members show stronger  $3\text{-}\mu\text{m}$  absorption than low-VDI counterparts, this would support the volatile-exposure interpretation. Conversely, if spectroscopic observations reveal no systematic differences, the VDI signal may simply trace recent mechanical resurfacing as in the silicate case, with the weaker correlation reflecting measurement limitations rather than distinct physics.

#### 5.4. Implications for Q-type Production and NEA Origins

The concentration of fresh signatures in massive families has implications for the origin of Q-type near-Earth asteroids (NEAs). [Binzel et al. \(2010\)](#) showed that Q-types are substantially over-represented among NEAs relative to the main belt, attributing this primarily to tidal resurfacing during planetary close approaches. Our findings suggest a complementary source: massive families with elevated collisional activity continuously produce fresh fragments that, upon resonance delivery to planet-crossing orbits, would present as Q-types before space weathering converts them to S-types on  $\sim\text{Myr}$  timescales. Whether collisional and tidal mechanisms contribute comparably to the observed NEA Q-type excess remains an open question.

Our results suggest that massive families (particularly Flora, Phocaea, and Eos) may serve as preferential source regions for fresh NEA material. Their elevated collision rates produce fresh fragments that, upon delivery to planet-crossing orbits via mean-motion and secular resonances, would appear as Q-types before space weathering converts them to S-types on  $\sim\text{Myr}$  timescales. Recent dynamical modeling of family-to-NEA transfer pathways ([Broz et al. 2024](#)) provides a quantitative framework that may be used to test whether high-VDI families contribute disproportionately to the fresh NEA population.

This prediction is testable through dynamical modeling of family-to-NEA transfer efficiency weighted by VDI. If correct, the Q-type fraction among NEAs originating from high-VDI families should exceed that from low-VDI families, after controlling for delivery efficiency. Spectroscopic surveys of NEAs with well-constrained source regions ([Bottke et al. 2005](#)) could provide empirical tests.

### 5.5. Potential Selection Effects

We consider whether the observed  $N$ -VDI correlation could arise from selection effects rather than physical processes:

(i) *Membership completeness*: Larger families have better-defined boundaries and more complete membership catalogs, potentially including more extreme outliers simply due to improved sampling statistics. However, our VDI metric is normalized by family size ( $N_{fresh}/N_{total}$ ), which should eliminate this effect. Additionally, if completeness drove the correlation, we would expect it to weaken for the most populous families where catalogs are essentially complete, instead, the correlation strengthens.

(ii) *Photometric depth*: Massive families contain more bright members with potentially higher signal-to-noise ratio measurements. We tested this by restricting the sample to  $H < 15$  mag (ensuring uniform photometric quality) and found consistent correlations ( $r_s = 0.45$ ,  $p < 10^{-5}$ ).

(iii) *Family definition circularity*: If family membership algorithms preferentially include spectrally similar objects, VDI could be artificially suppressed in all families. This would work *against* our observed trend (suppressing variance uniformly), strengthening confidence that the size-dependent signal is genuine.

(iv) *VDI as noise proxy*: One might worry that large families simply have more noisy measurements in the tail. However, the AKARI cross-validation demonstrates that family averaging *reduces* scatter, and the  $D \geq 5$  km control (Table 4) shows the correlation remains significant even for large bodies with the best photometry ( $r_s = 0.496$ ,  $p < 10^{-3}$ )—inconsistent with a noise-driven explanation.

### 5.6. Sensitivity Analysis

Table 4 summarizes comprehensive sensitivity tests. Key findings include:

- **Threshold Robustness**: Higher thresholds strengthen correlations (Figure 10), validating the interpretation that extreme values trace recent activity. The threshold-dependence of correlation strength (Table 4:  $r_s = 0.353$  at threshold 1.0 vs.  $r_s = 0.476$  at 1.2) demonstrates that VDI is not critically sensitive to the specific cutoff value. Alternative tail-statistics definitions (e.g., top 0.5% vs. 0.2% percentile) yield consistent positive correlations, confirming that the signal reflects real tail-weight differences rather than threshold artifacts.

- **Diameter Dependence**: The correlation remains significant even for large bodies ( $D \geq 5$  km,  $r_s = 0.496$ ,  $p < 10^{-3}$ ), demonstrating that the size-VDI relationship is not solely driven by Yarkovsky-affected small debris (Figure 11).

- **Heliocentric Consistency**: Inner belt ( $r_s = 0.591$ , 95% CI: [0.33, 0.76]) and outer belt ( $r_s = 0.473$ , 95% CI: [0.32, 0.60]) subsamples both show significant correlations with overlapping confidence intervals, confirming that the signal is not an artifact of Yarkovsky drift efficiency variations.

### 5.7. Percentile Sensitivity Analysis

The choice of VDI threshold (99.8th percentile,  $p_V/p_{IR} > 1.2$ ) represents a balance between isolating statistically fresh surfaces and maintaining statistical power. To validate this selection and test the robustness of our conclusions, we performed systematic threshold variation analysis across five percentile levels (95th–99.8th percentile of the main-belt ratio distribution).

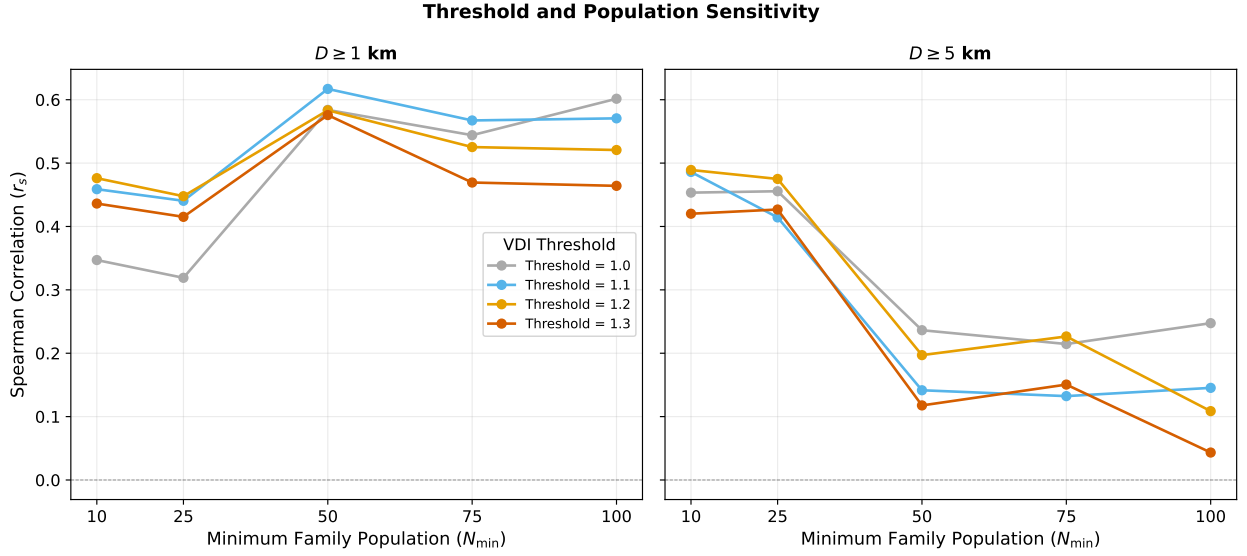


**Figure 10. Threshold and Population Sensitivity.** Spearman correlation ( $r_s$ ) as a function of minimum family population ( $N_{\min}$ ) for four VDI thresholds (1.0, 1.1, 1.2, 1.3) and two diameter cuts ( $D \geq 1$  km, left;  $D \geq 5$  km, right). For  $D \geq 1$  km, the signal is robust across all  $N_{\min}$  values and higher thresholds consistently yield stronger correlations. For  $D \geq 5$  km, the correlation weakens at  $N_{\min} \geq 50$  due to sample size reduction (from  $n = 97$  at  $N_{\min} = 10$  to  $n \lesssim 20$  at  $N_{\min} = 50$ ) rather than loss of the physical signal. The baseline result ( $r_s = 0.496$ , Table 4) corresponds to  $N_{\min} = 10$ .

**Table 4. Sensitivity Analysis Summary.** Spearman correlation ( $r_s$ ) across varying parameters. Bootstrap 95% confidence intervals are provided for heliocentric subsamples. The overlapping CIs confirm regional consistency.

Scenario	Thresh.	$N_{fam}$	$r_s$	$p$ -value	95% CI
Baseline ( $D \geq 1$ )	1.2	154	0.476	$4.31 \times 10^{-10}$	—
High Pop. ( $N \geq 50$ )	1.2	82	0.587	$6.64 \times 10^{-9}$	—
Lower Threshold	1.0	154	0.353	$6.57 \times 10^{-6}$	—
Inner Belt ( $a < 2.5$ )	1.2	26	0.591	$1.47 \times 10^{-3}$	[0.33, 0.76]
Outer Belt ( $a \geq 2.5$ )	1.2	129	0.473	$1.51 \times 10^{-8}$	[0.32, 0.60]
Large Body ( $D \geq 5$ )	1.2	97	0.496	$< 10^{-3}$	—

Table 5 presents correlation strengths as a function of threshold level. Correlation strength increases monotonically from  $r_s = 0.104$  (95th percentile, non-significant) to  $r_s = 0.487$  (99.8th percentile,  $p < 10^{-10}$ ), spanning a variation of  $\Delta r_s = 0.38$ . This threshold-dependence reveals a fundamental property of the VDI metric: only extreme thresholds (above the 99th percentile) successfully isolate rare resurfacing events from photometric scatter.

The strong threshold-dependence demonstrates that VDI detects *rare* collisional rejuvenation rather than bulk population properties. Lower thresholds (95th–98th percentile) capture moderate albedo variations dominated by measurement noise and minor compositional heterogeneity, yielding weak correlations ( $r_s < 0.15$ ,  $p > 0.10$ ). Only at extreme thresholds (99th+ percentile) does the signal emerge, consistent with a model where statistically anomalous freshness signatures trace recent ( $< \tau_{sw}$ ) resurfacing events that are inherently rare within weathered populations.

The 99.8th percentile threshold ( $p_V/p_{IR} > 1.2$ ) optimizes this trade-off: it maximizes correlation strength while retaining sufficient fresh-object detections ( $n_{\text{fresh}} = 275$  in the threshold-scan analysis; see Table 5 note for the minor difference from the pipeline value of 246) for statistically robust family-level VDI estimates. Alternative thresholds yield qualitatively consistent positive correlations, confirming that the signal is not an artifact of the specific cutoff value but reflects real tail-weight differences between large and small families.

**Table 5. Percentile Sensitivity Analysis.** Spearman correlation as a function of threshold level. Bold row: adopted threshold.

Percentile	Threshold	$N_{\text{fresh}}$	$r_s$	$p$
95.0th	0.714	6165	0.104	0.197
98.0th	0.757	2458	0.122	0.131
99.0th	0.904	1226	0.377	$1.3 \times 10^{-6}$
99.5th	1.043	615	0.438	$1.3 \times 10^{-8}$
99.8th (adopted)	1.218	246	0.487	$1.3 \times 10^{-10}$

Note:  $N_{\text{fresh}}$ : total asteroids exceeding the threshold across all 154 families.

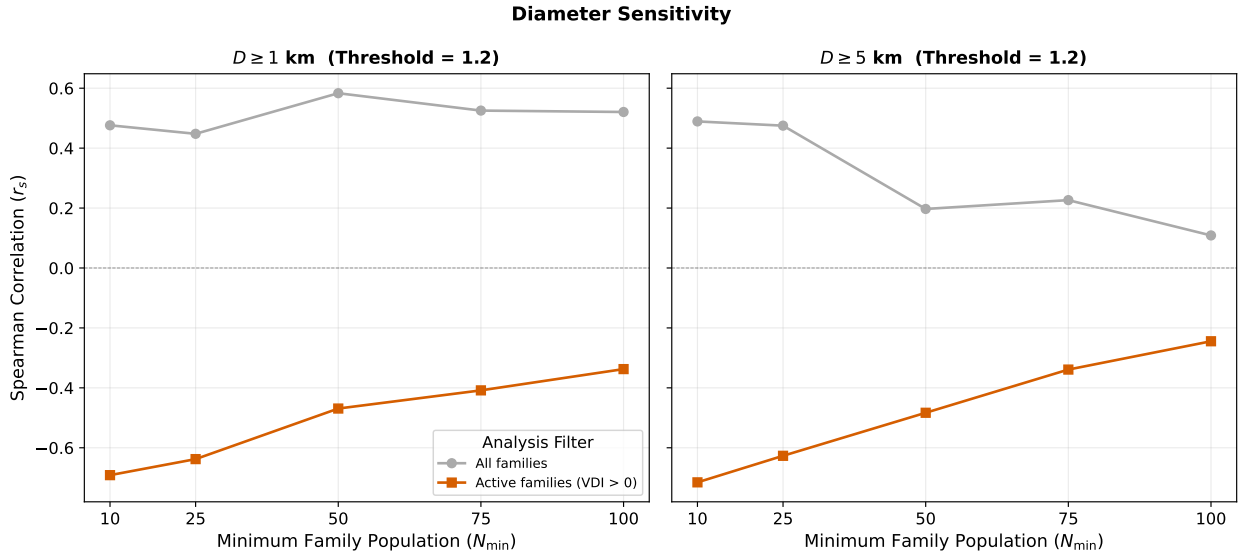


**Figure 11. Diameter Sensitivity.** Grey circles: correlation across all families at threshold 1.2. The “All families” line confirms the signal for  $D \geq 5 \text{ km}$  at  $N_{\min} = 10$  ( $r_s = 0.496$ ,  $p < 10^{-3}$ ), demonstrating that the size–VDI relationship is not driven solely by small Yarkovsky-affected debris. At higher  $N_{\min}$  the signal weakens due to reduced sample size (see Figure 10). Orange squares: restricting to families with  $\text{VDI} > 0$  produces a negative correlation, which is a mechanical consequence of VDI’s normalization ( $N_{\text{total}}$  in the denominator suppresses VDI in large families) and does not reflect a physical anti-correlation.

## 5.8. Scope and Limitations of Claims

To clarify the scope of our findings and anticipate potential misinterpretations, we explicitly state what this analysis does and does not demonstrate:

### 5.8.1. What We Claim

- A strong statistical correlation exists between family population size  $N$  and VDI across the sampled main-belt families ( $r_s = 0.476$ ,  $p = 4.31 \times 10^{-10}$ ).
- This correlation survives multiple control tests (age-matched contrasts, heliocentric splits, diameter cuts) and cannot be explained by  $N$ -dependent variance in binomial sampling alone.
- The observed pattern is consistent with population-dependent collisional resurfacing as the dominant driver, though alternative or contributing mechanisms cannot be excluded.

### 5.8.2. What We Do NOT Claim

- Causality: We do not establish that  $N$  directly *causes* elevated VDI. The correlation demonstrates statistical association, not causal determination.
- Unique Mechanism: We do not rule out alternative or contributing processes such as YORP-driven mass shedding, tidal encounters, or thermal cycling effects.

- **Areal Coverage:** VDI measures the *incidence rate* of extreme freshness signatures (tail statistics), not the fractional surface area of fresh material.
- **Universal Applicability:** Our results apply to the sampled main-belt family population ( $N \geq 10$ ,  $D \geq 1$  km) and may not generalize to smaller families, near-Earth asteroids, or trans-Neptunian objects without independent validation.
- **Physical Calibration:** The empirical scaling exponent  $\alpha \approx 0.5$  is a statistical descriptor, not a theoretically derived or experimentally calibrated parameter.

## 5.9. Limitations and Future Directions

Several limitations should be noted:

1. **NEOWISE Systematics:** While family averaging suppresses random errors, systematic biases correlated with family properties (e.g., phase angle coverage varying with heliocentric distance) cannot be fully excluded. Recent reanalyses (Masiero et al. 2020) demonstrate improved calibration but residual systematics remain at the  $\sim 10\%$  level.
2. **Classification Dependence:** Results depend on the adopted family classification framework (Nesvorný et al. 2015); membership uncertainties may affect small families preferentially.
3. **Physical Pathway:** Our analysis constrains statistical relationships but does not uniquely determine physical mechanisms. Dynamical modeling incorporating family-specific collision rates, velocity dispersions, and size-frequency distributions is needed to test the collisional interpretation quantitatively.
4. **Alternative Resurfacing Mechanisms:** While we focus on collisional resurfacing, other processes may contribute. YORP-driven spin-up and mass shedding (Delbo et al. 2017) can expose fresh subsurface material on rubble-pile asteroids. Tidal encounters during planetary close approaches may also cause surface disturbances, particularly for near-Earth asteroid precursors. Separating these contributions requires combined photometric, spectroscopic, and rotational state analysis.
5. **Yarkovsky Control:** The  $D \geq 1$  km cut and heliocentric split provide partial control, but taxon-specific thermal properties remain a potential complication for detailed cross-taxonomic comparisons.
6. **Carbonaceous Interpretation:** The physical meaning of “freshness” in C-complex asteroids remains uncertain and may differ fundamentally from the silicate case.

Future work should prioritize: (i) spectroscopic follow-up of high-VDI members in both S- and C-complex families to constrain surface composition; (ii) dynamical simulations of family collision rates to test whether the  $N$ -VDI correlation matches theoretical predictions; (iii) extension to smaller diameter ranges using next-generation surveys (e.g., Rubin Observatory LSST) to probe the size-dependence of the resurfacing signal; and (iv) detailed case studies of potential outliers (e.g., large families with anomalously low VDI or small families with elevated freshness) to identify boundary conditions where the population-size proxy breaks down.

## 6. CONCLUSION

Using family-level statistical aggregation to suppress observational noise, we report a robust correlation between asteroid family population size and fresh surface signatures:

1. **Statistical Pattern:** The size–VDI correlation ( $r_s = 0.476$ ,  $p = 4.31 \times 10^{-10}$ ) persists across taxonomic types within the sampled main-belt population, surviving Monte Carlo significance tests, age-matched controls, and heliocentric independence tests. Binomial null model simulations confirm that the observed correlation (exceeding the 99.99th percentile of null distributions for  $p_0 \geq 0.05$ ) cannot be explained by N-dependent variance in binomial sampling alone.

2. **Size vs. Age:** Among tested parameters (population size, age, heliocentric distance, taxonomy), family population size emerges as the strongest statistical correlate of fresh surface incidence in evolved families, with the effect persisting in age-matched comparisons of ancient ( $> 2$  Gyr) populations.

3. **Model Consistency:** The observed pattern is consistent with population-dependent collisional resurfacing maintaining elevated regolith gardening rates in massive families. However, this analysis establishes a statistical benchmark for dynamical models rather than uniquely constraining the physical mechanism.

This work demonstrates that family-scale statistical analysis can recover surface evolution signals from noisy photometric surveys where individual-object studies have struggled. The approach provides an observational constraint for testing collision rate predictions from dynamical models and may be applicable to other stochastic planetary processes where population-level aggregation reveals trends obscured by measurement uncertainty.

Massive families represent promising targets for identifying fresh Q-type material and may contribute significantly to the near-Earth asteroid population through ongoing collisional activity. The Flora, Phocaea, and Eos families, in particular, require detailed spectroscopic characterization of their high-VDI members.

## REFERENCES

- Binzel R. P., et al., 2010, *Nature*, 463, 331
- Bottke W. F., Durda D. D., Nesvorný D., Jedicke R., Morbidelli A., Vokrouhlický D., Levison H. F., 2005, *Icarus*, 179, 63
- Brož M., et al., 2024, *Astronomy & Astrophysics*, 689, A183
- Brunetto R., et al., 2015, in Michel P., DeMeo F. E., Bottke W. F., eds., Asteroids IV. University of Arizona Press, Tucson, pp 597–616
- Cook R. D., 1977, *Technometrics*, 19, 15
- DeMeo F. E., Binzel R. P., Slivan S. M., Bus S. J., 2009, *Icarus*, 202, 160
- Delbo M., et al., 2017, *Science*, 357, 1026
- Durda D. D., Bottke W. F., Nesvorný D., Enke B. L., Merline W. J., Asphaug E., Richardson D. C., 2007, *Icarus*, 186, 498
- Lantz C., Brunetto R., Barucci M. A., Fornasier S., Baklouti D., Binzel R. P., DeMeo F. E., 2018, *Icarus*, 302, 10
- Loeffler M. J., Dukes C. A., Baragiola R. A., 2009, *Journal of Geophysical Research: Planets*, 114, E03003
- Mainzer A., et al., 2011, *The Astrophysical Journal*, 731, 53
- Masiero J. R., et al., 2020, *The Planetary Science Journal*, 1, 9
- Nesvorný D., Brož M., Carruba V., 2015, in Michel P., DeMeo F. E., Bottke W. F., eds., Asteroids IV. University of Arizona Press, Tucson, pp 297–321
- Parker A., Ivezić Z., Juric M., Lupton R., Sekora M. D., Kowalski A., 2008, *Icarus*, 198, 138
- Richardson J. E., Melosh H. J., Greenberg R. J., 2004, *Science*, 306, 1526
- Sasaki S., Nakamura K., Hamabe Y., Kurahashi E., Hiroi T., 2001, *Nature*, 410, 555
- Sergeyev A. V., Carry B., 2021, *Astronomy & Astrophysics*, 652, A59
- Spoto F., Milani A., Knežević Z., 2015, *Icarus*, 257, 275
- Usui F., et al., 2011, *Publications of the Astronomical Society of Japan*, 63, 1117

## Kaplan

Vernazza P., Binzel R. P., Rossi A., Fulchignoni M., Birlan M., 2009, [Nature](#), 458, 993

Willman M., Jedicke R., Moskovitz N., Nesvorný D., Vokrouhlický D., Mothé-Diniz T., 2010, [Icarus](#), 208, 758

This paper has been typeset from a  $\text{\TeX}/\text{\LaTeX}$  file prepared by the author.